Ferrochiral, antiferrochiral, and ferrichiral skyrmion crystals in an itinerant honeycomb magnet

Ryota Yambe [1] and Satoru Hayami [2]
[1]*Department of Applied Physics, The University of Tokyo, Tokyo 113-8656, Japan*
[2]*Graduate School of Science, Hokkaido University, Sapporo 060-0810, Japan*

(Received 9 August 2022; revised 5 January 2023; accepted 6 January 2023; published 23 January 2023)

Topological spin textures, such as a skyrmion crystal, are a source of unusual physical phenomena owing to the interplay between magnetism and topology. Since physical phenomena depend on the topological property and the symmetry of underlying spin structures, the search for new topological spin textures and emergent phenomena is one of the challenges in condensed matter physics. In this study, we theoretically explore topological spin textures arising from the synergy between spin, charge, and sublattice degrees of freedom in an itinerant magnet. By performing simulated annealing for an effective spin model of the honeycomb Kondo lattice model, we find a plethora of skyrmion crystal instabilities at low temperatures, whose topological spin textures are classified into three types: ferrochiral, antiferrochiral, and ferrichiral skyrmion crystals. We show that the obtained skyrmion crystals are the consequence of the spin-orbit-coupling-free honeycomb structure. Our results reveal the potential for itinerant honeycomb magnets to host a wide variety of skyrmion crystal and emergent phenomena.

DOI: 10.1103/PhysRevB.107.014417

I. INTRODUCTION

Noncoplanar spin structures with nontrivial topology (topological spin textures) have attracted much attention, since they give rise to fascinating physical phenomena arising from their emergent electromagnetic fields [1–5]. The most familiar topological spin texture is a skyrmion, whose topological property is characterized by the skyrmion number $N_{\rm sk} = pv$; p and v represent the polarity and vorticity of the skyrmion, respectively [1]. Since the different sets of $(p, v, N_{\rm sk})$ result in different types of skyrmions, as shown in Figs. 1(a)–1(f), they become a source of a variety of quantum transports and dynamics including the topological Hall and Nernst effects and skyrmion Hall effect [6–15].

The appearance of each skyrmion is dependent on a microscopic interaction. Specifically, the vorticity is determined by types of spin interactions. In centrosymmetric magnets, the competing exchange interactions in frustrated magnets lead to the crystal formation of the skyrmion (SkX) with $v = \pm 1$ [16–21], while the long-range higher-order exchange interaction in itinerant magnets favors the SkX with both $v = \pm 1$ and ± 2 depending on the magnetic field [5,22,23]. The degeneracy in terms of v is lifted by anisotropic exchange interactions originating from the spin-orbit coupling [24–27] or dipolar interactions [28,29]. Meanwhile, the polarity is determined by the magnetic field direction; $p = +1$ (-1) is favored under the field along the $-z$ $(+z)$ direction. In this way, a key essence of engineering $(p, v, N_{\rm sk})$ of the skyrmion has been clarified based on the microscopic interaction.

In the present study, we explore SkXs by focusing on the sublattice degree of freedom. The effect of the sublattice degree of freedom has been studied in the 120° three-sublattice structure on the triangular lattice [30], honeycomb structure [31,32], kagome structure [33], diamond structure [34], and multilayer structure [35–41]. One of the typical examples characteristic of the sublattice structure is the antiferromagnetic SkX on a bipartite lattice with sublattice $\alpha = {\rm A}, {\rm B}$, where sublattice A forms the SkX with $(p^{\rm A}, v^{\rm A}, N_{\rm sk}^{\rm A}) = (-1, +1, -1)$ in Fig. 1(a) and sublattice B forms that with $(p^{\rm B}, v^{\rm B}, N_{\rm sk}^{\rm B}) = (+1, +1, +1)$ in Fig. 1(b). In this case, no topological Hall effect occurs due to the staggered skyrmion number $N_{\rm sk}^{\rm A} = -N_{\rm sk}^{\rm B}$, while the topological spin Hall effect is expected [31].

To realize a variety of topological spin textures in multisublattice systems, we focus on the synergy among the spin, charge, and sublattice degrees of freedom in an itinerant magnet. By performing simulated annealing for an effective spin model of the honeycomb Kondo lattice model (KLM), we find that the synergy gives rise to five new SkXs with different $(N_{\rm sk}^{\rm A}, N_{\rm sk}^{\rm B})$: two antiferrochiral SkXs with

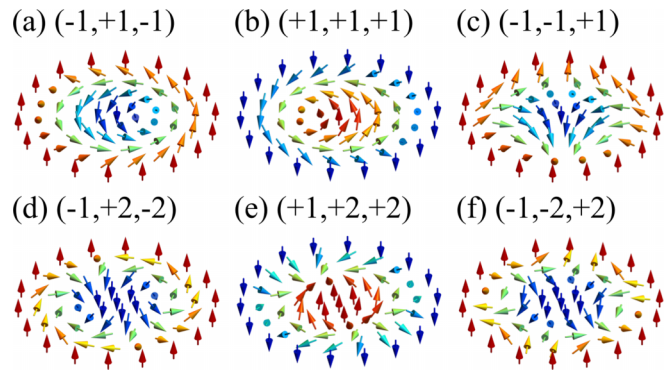

FIG. 1. Skyrmions characterized by $(p, v, N_{\rm sk})$. The arrow and color show the spin direction and z component, respectively, where red (blue) corresponds to the positive (negative) z component.

$(N_{\rm sk}^{\rm A}, N_{\rm sk}^{\rm B}) = (-1, +1)$ and $(-2, +2)$, two ferrochiral SkXs with $(N_{\rm sk}^{\rm A}, N_{\rm sk}^{\rm B}) = (-1, -1)$ and $(-2, -2)$, and a ferrichiral SkX with $(N_{\rm sk}^{\rm A}, N_{\rm sk}^{\rm B}) = (-1, +2)$.

The rest of this paper is organized as follows. In Sec. II, we introduce the effective spin model and the simulation method. The ground-state phase diagram in the model without (with) the magnetic field is shown in Sec. III A (Sec. III B). We summarize our results in Sec. IV. In addition, we show details of our results: derivation of the effective spin model in Appendix A, SkXs in models with different parameters in Appendix B, analytical calculation at zero field in Appendix C, and field-induced trivial phases in Appendix D.

II. MODEL AND METHOD

We consider the honeycomb lattice with sublattices A and B shown in the inset of Fig. 2(a). The effective spin model, which is obtained in the weak-coupling regime of the honeycomb KLM, is given by

$$\mathcal{H}^{\rm eff} = -2J \sum_{\eta} \Gamma_{\eta}(X) + 2\frac{K}{N} \sum_{\eta} \Gamma_{\eta}(X)^2, \tag{1}$$

where $\Gamma_{\eta}(X) = \sum_{\alpha,\beta} X^{\alpha\beta} \boldsymbol{S}_{\alpha\boldsymbol{Q}_{\eta}} \cdot \boldsymbol{S}_{\beta-\boldsymbol{Q}_{\eta}}$; $\boldsymbol{S}_{\alpha\boldsymbol{q}}$ with the wave vector $\boldsymbol{q}$ and sublattice $\alpha = {\rm A}, {\rm B}$ is the Fourier transform of the localized spin, $X^{\alpha\beta}$ represents the form factor of the interaction in terms of the sublattice, $X^{\rm AA} = X^{\rm BB}$ and $X^{\rm AB} = (X^{\rm BA})^*$, and N is the number of unit cells. The first term represents the bilinear interaction with $J > 0$, which corresponds to the Ruderman-Kittel-Kasuya-Yosida (RKKY) interaction [42–44]. We only consider the dominant contributions at specific $\boldsymbol{Q}_{\eta}$, which gives the largest eigenvalue of the bare magnetic susceptibility of itinerant electrons in momentum space. We choose threefold symmetric ordering vectors so as to satisfy the honeycomb lattice symmetry: $\boldsymbol{Q}_1 = (0, \pi/3)$, $\boldsymbol{Q}_2 = (-\sqrt{3}\pi/6, -\pi/6)$, and $\boldsymbol{Q}_3 = (\sqrt{3}\pi/6, -\pi/6)$, where we set the lattice constant as unity. Then, the form factor satisfies $X^{\alpha\beta} = (X^{\alpha\beta})^*$ due to the mirror symmetry with respect to the xz plane [27]. The second term represents the positive biquadratic interaction with $K > 0$, which corresponds to the higher-order RKKY interaction and tends to favor noncoplanar spin textures including the SkX [5,22,23,45]. The derivation of the effective spin model is shown in Appendix A.

In contrast to the previous effective spin model for the triangular KLM [23], the present model includes the effect of the intersublattice RKKY and biquadratic interactions owing to the multisublattice honeycomb structure. Thus, the present model can describe the multiple-Q instability that arises from the synergy between the spin, charge, and sublattice degrees of freedom. In the following, we study the general case of the interactions by setting $X^{\rm AA} \equiv \cos^2\Theta$ and $X^{\rm AB} \equiv \pm\sin^2\Theta$ while changing Θ $(0 < \Theta \leqslant \pi/2)$ as well as K. We set $J = 1$ as the energy unit. It is noted that the form factors in the first and second terms in Eq. (1) are usually different from each other, while the results are qualitatively similar even when considering different form factors (see Appendix B).

First, we discuss the ground state at $K = 0$. Then, the model in Eq. (1) exhibits the instability toward the single-Q spiral state on each sublattice irrespective of Θ. When $X^{\rm AB} \neq 0$ $(\Theta > 0)$, both spirals are characterized by the same $\boldsymbol{Q}_{\eta}$ and the same spiral plane for both positive and negative $X^{\rm AB}$. The sign dependence of $X^{\rm AB}$ is found in the relative spiral angle; the B spin at $\boldsymbol{R}_{{\rm B}i}$ is (anti)parallel to the A spin at $\boldsymbol{R}_{{\rm B}i} + \boldsymbol{d}_{\eta}^*$ for positive (negative) $X^{\rm AB}$, where $\boldsymbol{R}_{{\rm B}i}$ is the position vector at site i on sublattice B and $\boldsymbol{d}_{\eta}^*$ $(\boldsymbol{d}_{\eta}^* \cdot \boldsymbol{Q}_{\eta} = 0)$ is the displacement vector for three nearest-neighbor bonds shown in the inset of Fig. 2(a). In other words, positive (negative) $X^{\rm AB}$ tends to favor the (anti)ferromagnetic spin alignment for sublattices A and B.

Next, to investigate the ground state for nonzero K, we perform simulated annealing combined with the standard Metropolis local updates for the system size with $N = 36^2$. We gradually reduce the temperature with a rate $T_{n+1} = \alpha T_n$, where T_n is the temperature at the nth step. We set the initial temperature $T_0 = 1$ and the coefficient $\alpha \approx 0.999539589$. A final temperature $T_{\rm f} = 0.01$ is reached after a total of 10^6 Monte Carlo steps (MCSs), where we perform 10^2 MCSs at each temperature T_n. The following results are obtained by using other α and the number of MCSs unless α is much smaller than 1. After 10^5 MCSs for the thermalization at $T_{\rm f}$, we perform 10^6 MCSs for measurements, where 10^4 samples are used for average. To determine the phase boundary, we set the spin configuration obtained near the phase boundary as the initial spin configuration and perform the simulated annealing starting at low temperatures ($T_0 = 0.02$–0.05).

We identify magnetic phases from the spin structure factor, magnetization, spin scalar chirality, and skyrmion number in each sublattice. The spin structure factor for sublattice $\alpha = {\rm A}, {\rm B}$ is defined as

$$S^{\mu}(\alpha, \boldsymbol{q}) = \left\langle \frac{1}{N} \sum_{j,k} S_{\alpha j}^{\mu} S_{\alpha k}^{\mu} e^{i\boldsymbol{q}\cdot(\boldsymbol{R}_{\alpha j} - \boldsymbol{R}_{\alpha k})} \right\rangle, \tag{2}$$

where $\mu = x, y, z$, $\boldsymbol{R}_{\alpha j}$ is the position vector at site j on sublattice α, N is the number of unit cells, and $\langle \cdots \rangle$ is the average over the Monte Carlo samples. We also calculate the in-plane spin structure factor, $S^{\perp}(\alpha, \boldsymbol{q}) = S^{x}(\alpha, \boldsymbol{q}) + S^{y}(\alpha, \boldsymbol{q})$. The magnetization for sublattice α is defined as

$$M_{\alpha} = \left\langle \frac{1}{N} \sum_{j} S_{\alpha j}^{z} \right\rangle. \tag{3}$$

The local spin scalar chirality of the triangle on sublattice α is defined as

$$\chi_{\alpha \boldsymbol{r}} = \boldsymbol{S}_{\alpha j} \cdot (\boldsymbol{S}_{\alpha k} \times \boldsymbol{S}_{\alpha l}), \tag{4}$$

where the position vector $\boldsymbol{r}$ represents the triangle center and the triangle consists of (j, k, l) sites labeled in counterclockwise order. The uniform spin scalar chirality of sublattice α is given by

$$\chi_{\alpha}^{\rm sc} = \left\langle \frac{1}{N} \sum_{\boldsymbol{r}} \chi_{\alpha \boldsymbol{r}} \right\rangle. \tag{5}$$

The skyrmion density at the triangle $\boldsymbol{r}$ on sublattice α [46] is defined as

$$\tan\left(\frac{\Omega_{\alpha \boldsymbol{r}}}{2}\right) = \left[\frac{\boldsymbol{S}_{\alpha j} \cdot (\boldsymbol{S}_{\alpha k} \times \boldsymbol{S}_{\alpha l})}{1 + \boldsymbol{S}_{\alpha j} \cdot \boldsymbol{S}_{\alpha k} + \boldsymbol{S}_{\alpha k} \cdot \boldsymbol{S}_{\alpha l} + \boldsymbol{S}_{\alpha l} \cdot \boldsymbol{S}_{\alpha j}} \right]. \tag{6}$$

Then, the skyrmion number for sublattice α is given by

$$N_{\rm sk}^{\alpha} = \frac{1}{4\pi N_{\rm m}} \left\langle \sum_{\boldsymbol{r}} \Omega_{\alpha \boldsymbol{r}} \right\rangle, \tag{7}$$

where $N_{\rm m}$ is the number of magnetic unit cells.

To judge whether the obtained spin configurations are topologically nontrivial, we compute a total skyrmion number ($N_{\rm sk}^{\rm tot}$) and a staggered skyrmion number ($N_{\rm sk}^{\rm stagg}$) as

$$N_{\rm sk}^{\rm tot} = \left| N_{\rm sk}^{\rm A} + N_{\rm sk}^{\rm B} \right|, \tag{8}$$

$$N_{\rm sk}^{\rm stagg} = \left| N_{\rm sk}^{\rm A} - N_{\rm sk}^{\rm B} \right|. \tag{9}$$

By using them, we categorize a topological property into four types: ferrochiral (FC) SkX with $N_{\rm sk}^{\rm tot} \neq 0$ and $N_{\rm sk}^{\rm stagg} = 0$, antiferrochiral (AFC) SkX with $N_{\rm sk}^{\rm tot} = 0$ and $N_{\rm sk}^{\rm stagg} \neq 0$, ferrichiral (FerriC) SkX with $N_{\rm sk}^{\rm tot} \neq 0$ and $N_{\rm sk}^{\rm stagg} \neq 0$, and trivial states with $N_{\rm sk}^{\rm tot} = 0$ and $N_{\rm sk}^{\rm stagg} = 0$.

III. RESULTS

A. Zero-field phase diagram

Figure 2(a) shows the phase diagram on the Θ-K ($|X^{\rm AB}|$-K) plane obtained by simulated annealing. By introducing K, the single-Q spiral state shows the instabilities toward three multiple-Q states: chiral stripe (CS) I, CS II, and FC (AFC) SkX II for positive (negative) $X^{\rm AB}$. The spin configurations of two CS states are characterized by a double-Q superposition of the spiral wave at $\boldsymbol{Q}_{\alpha}^{\rm spiral} \equiv \boldsymbol{Q}_{\eta}$ and the sinusoidal wave at $\boldsymbol{Q}_{\alpha}^{\rm sin} \equiv \boldsymbol{Q}_{\eta'}$ ($\eta \neq \eta'$) in each sublattice α [23,47–49]. Although their sinusoidal component is the same for sublattices A and B in both CS states, i.e., $\boldsymbol{Q}_{\rm A}^{\rm sin} = \boldsymbol{Q}_{\rm B}^{\rm sin}$, the spiral components are different from each other: $\boldsymbol{Q}_{\rm A}^{\rm spiral} \neq \boldsymbol{Q}_{\rm B}^{\rm spiral}$ for CS I and $\boldsymbol{Q}_{\rm A}^{\rm spiral} = \boldsymbol{Q}_{\rm B}^{\rm spiral}$ for CS II. The CS states are the trivial states without $N_{\rm sk}^{\rm tot}$ and $N_{\rm sk}^{\rm stagg}$.

Meanwhile, FC (AFC) SkX II appears for $K \gtrsim 0.095$ and positive (negative) $X^{\rm AB}$, which indicates that a nonzero but small $\Theta \gtrsim 15.5\pi/240$ ($|X^{\rm AB}| \gtrsim 0.041$) is enough to stabilize the SkXs. In both SkXs, the spin configurations on each sublattice are characterized by the triangular lattice of the skyrmion, while the constituent skyrmions are different, as shown in Figs. 2(b) and 2(c): $(p^{\alpha}, v^{\alpha}, N_{\rm sk}^{\alpha}) = (-1, +2, -2)$ for $\alpha = {\rm A}, {\rm B}$ [Fig. 1(d)] in FC SkX II and $(p^{\rm A}, v^{\rm A}, N_{\rm sk}^{\rm A}) = (+1, +2, +2)$ [Fig. 1(e)] and $(p^{\rm B}, v^{\rm B}, N_{\rm sk}^{\rm B}) = (-1, +2, -2)$ [Fig. 1(d)] in AFC SkX II. In the end, FC SkX II has the uniform skyrmion number as $N_{\rm sk}^{\rm tot} = 4$ and $N_{\rm sk}^{\rm stagg} = 0$, whereas AFC SkX II has the staggered skyrmion number as $N_{\rm sk}^{\rm tot} = 0$ and $N_{\rm sk}^{\rm stagg} = 4$. The key ingredients for FC and AFC SkX II are the (anti)ferromagnetically coupled bipartite structure and itinerant nature giving nonzero positive K. We find that AFC SkX II is regarded as the antiferromagnetic SkX since the opposite sign on the skyrmion number arises from the opposite polarity. Note that such an antiferromagnetic SkX with a high topological number has not been found so far. Furthermore, our mechanism does not require a multilayer structure to stabilize the antiferromagnetic SkX [31,50]. The phase diagram in Fig. 2(a) is discussed by using analytical calculations based on the spin ansatz in each phase in Appendix C.

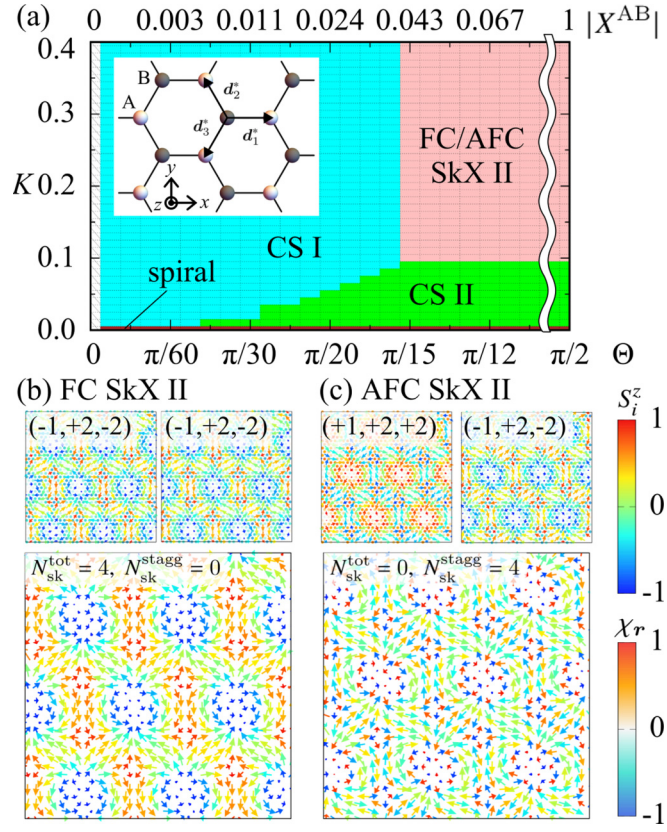

FIG. 2. (a) Phase diagram on the Θ-K ($|X^{\rm AB}|$-K) plane at $T = 0.01$. CS, FC SkX, and AFC SkX represent the chiral stripe state, ferrochiral SkX, and antiferrochiral SkX, respectively. Inset: The honeycomb structure with sublattices A (white) and B (gray). $\boldsymbol{d}_{\eta}^{*}$ ($\eta = 1$–3) is the vector of three nearest-neighbor bonds. Snapshots of the (b) FC and (c) AFC SkXs II at $\Theta = \pi/12$ and $K = 0.4$. Upper left (right) panel: Spin ($\boldsymbol{S}_i$) and chirality ($\chi_{\boldsymbol{r}}$) configurations on sublattice A (B). Lower panel: Spin configuration on the honeycomb lattice. The arrows, contours of arrows, and contours of circles show the xy spin component, z spin components, and spin scalar chirality, respectively. $(p^{\alpha}, v^{\alpha}, N_{\rm sk}^{\alpha})$ and $(N_{\rm sk}^{\rm tot}, N_{\rm sk}^{\rm stagg})$ are shown in the upper and lower panels, respectively.

B. Finite-field phase diagram

We further show rich topological spin textures by introducing the magnetic-field term $\mathcal{H}^{\rm Zeeman} = -H \sum_{\alpha,i} S_{\alpha i}^{z}$, where we set $H > 0$ favoring the negative polarity of the skyrmion. Figure 3(a) shows the Θ-H phase diagram at fixed $X^{\rm AB} < 0$ and $K = 0.4$. We find multiple SkX instabilities driven by the magnetic field for $\Theta \leqslant \pi/4$ ($|X^{\rm AB}| \leqslant 0.5$): FC SkX I, AFC SkX I, and FerriC SkX. We discuss the details of the spin configurations in each field-induced SkX in the following. We detail the other trivial phases denoted as I–V in Appendix D.

FC SkX I is constituted of the skyrmion with $(p^{\alpha}, v^{\alpha}, N_{\rm sk}^{\alpha}) = (-1, +1, -1)$ [Fig. 1(a)] for both sublattices ($\alpha = {\rm A}, {\rm B}$), as shown in Fig. 3(b), whose vorticity and the skyrmion number are halved compared to FC SkX II in Fig. 2(b), i.e., $N_{\rm sk}^{\rm tot} = 2$ and $N_{\rm sk}^{\rm stagg} = 0$. Meanwhile, FC SkX I is stabilized even for negative $X^{\rm AB}$, which is qualitatively in contrast to FC SkX II stabilized only for positive $X^{\rm AB}$. The emergence of FC SkX I is due to the different skyrmion

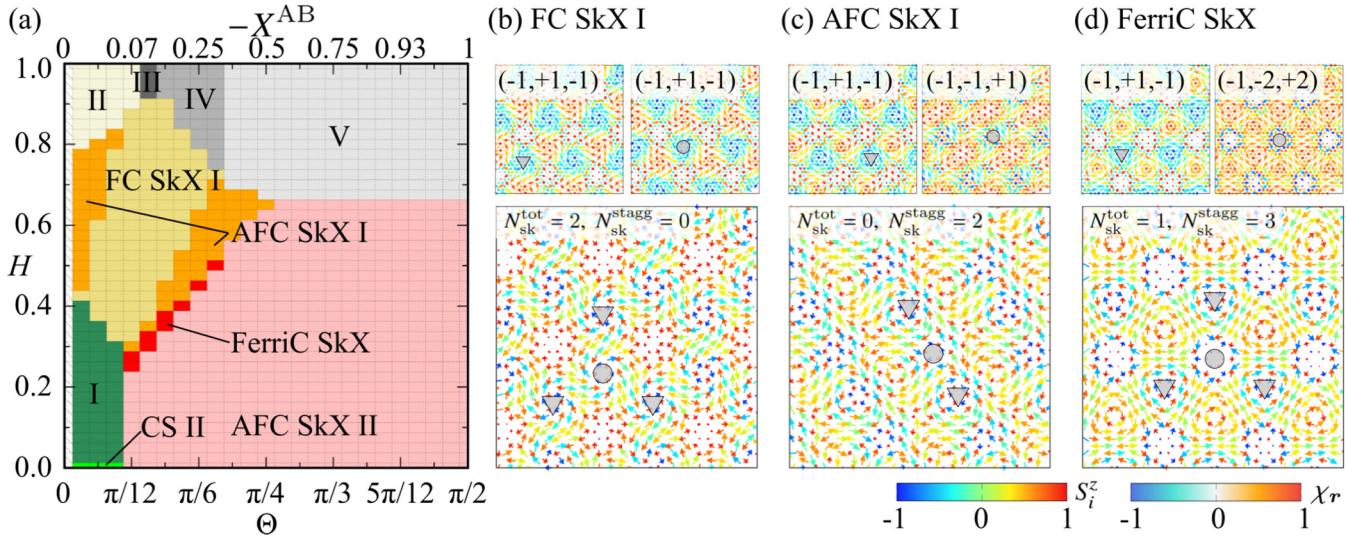

FIG. 3. (a) Phase diagram on the Θ-H plane at $X^{AB} < 0$, $K = 0.4$, and $T = 0.01$. FC SkX, AFC SkX, and FerriC SkX represent the ferrochiral SkX, antiferrochiral SkX, and ferrichiral SkX, respectively. I–V are nontopological phases. Snapshots of (b) FC SkX I at $\Theta = \pi/8$ and $H = 0.5$, (c) AFC SkX I at $\Theta = \pi/8$ and $H = 0.4$, and (d) FerriC SkX at $\Theta = \pi/8$ and $H = 0.375$, which corresponds to Figs. 2(b) and 2(c).

core positions to gain the energy by JX^{AB}; the skyrmion core at sublattice B represented by the circle is separated from that at sublattice A by the triangle so as to form the honeycomb network, as shown in Fig. 3(b). A similar shift of core positions has been found in three-sublattice SkXs in the antiferromagnetic triangular and kagome systems [30,33].

AFC SkX I consists of the skyrmions with $(p^A, v^A, N_{sk}^A) = (-1, +1, -1)$ [Fig. 1(a)] and $(p^B, v^B, N_{sk}^B) = (-1, -1, +1)$ [Fig. 1(c)], as shown in Fig. 3(c), which results in $N_{sk}^{tot} = 0$ and $N_{sk}^{stagg} = 2$. In contrast to AFC SkX II, the opposite sign of N_{sk}^{α} in AFC SkX I is owing to the opposite vorticity in the constituent skyrmions instead of the polarity; the A-sublattice SkX is characterized by the skyrmion spin texture with $v^A = +1$, while the B-sublattice one is described by the antiskyrmion spin texture with $v^B = -1$ in the upper panels of Fig. 3(c). Thus, AFC SkX I is regarded as a coexisting state of the skyrmion and antiskyrmion, where they are degenerate in the present model without the spin-orbit coupling. Although the domain structure of the skyrmion and antiskyrmion has been found [16,21], their coexisting ordered state has not been discovered without the multilayer structure so far [38]. The (anti)skyrmion cores in AFC SkX I are aligned in a one-dimensional way, breaking the threefold rotational symmetry.

The FerriC SkX sandwiched by AFC SkX II and AFC SkX I is formed by the skyrmions with $(p^A, v^A, N_{sk}^A) = (-1, +1, -1)$ [Fig. 1(a)] and $(p^B, v^B, N_{sk}^B) = (-1, -2, +2)$ [Fig. 1(f)], as shown in Fig. 3(d). Thus, this state has nonzero $N_{sk}^{tot} = 1$ and $N_{sk}^{stagg} = 3$ with a ferritype alignment of N_{sk}^{α}. The appearance of the FerriC SkX might be owing to the multisublattice system in itinerant magnets since the SkX with $|N_{sk}^{\alpha}| = 2$ is only realized for nonzero K. Indeed, such instability has not been reported in the isotropic localized spin model. The FerriC SkX is quite different from the other sublattice SkXs reported in the present study and previous studies: In the previous findings, the spin configurations on each sublattice are usually energetically degenerate, while the FerriC SkX consists of two SkXs with different energy. The stabilization of this novel intermediate state between AFC SkX I and AFC SkX II is a consequence of the competition between the effective spin interactions and Zeeman effect: The former tends to favor the SkX with $|N_{sk}| = 2$, while the latter tends to favor the SkX with $|N_{sk}| = 1$ [22,51].

IV. SUMMARY

To summarize, we theoretically propose a rich variety of SkXs in the itinerant honeycomb magnet by the synergy of the spin, charge, and sublattice degrees of freedom. By constructing the ground-state phase diagram of the effective spin model for the honeycomb KLM, we find five topological spin textures with different topological properties: ferrochiral SkXs I and II, antiferrochiral SkXs I and II, and ferrichiral SkX. We demonstrate that the essence lies in the competition among the bilinear interaction between different sublattices, positive biquadratic interaction, and magnetic field. Since the total (staggered) skyrmion number is closely related to the emergence of the topological Hall (spin Hall) effect, one expects a variety of transport phenomena driven by the emergent electromagnetic field. The important conditions to induce the present multiple SkX instabilities are the positive biquadratic interaction arising from the itinerant nature, the bipartite lattice structure, and the negligibly small spin-orbit coupling. These conditions imply that itinerant magnets with other bipartite lattice structure are also candidates for topological spin textures, such as an antiferromagnetic hedgehog lattice in the diamond structure.

ACKNOWLEDGMENTS

This research was supported by JSPS KAKENHI Grants No. JP21H01037, No. JP22H04468, No. JP22H00101, and No. JP22H01183, and by JST PRESTO (Grant No.

JPMJPR20L8). R.Y. was supported by Forefront Physics and Mathematics Program to Drive Transformation (FoPM). Parts of the numerical calculations were performed in the supercomputing systems in ISSP, the University of Tokyo.

APPENDIX A: DERIVATION OF THE EFFECTIVE SPIN INTERACTIONS

We derive the effective spin model in Eq. (1) in the main text by starting from the honeycomb KLM. The honeycomb KLM is given by

$$\mathcal{H}^{\mathrm{KLM}} = -\sum_{\alpha,\beta}\sum_{i,j,\sigma} t_{ij}^{\alpha\beta} c_{\alpha i\sigma}^{\dagger} c_{\beta j\sigma} + J_{\mathrm{K}} \sum_{\alpha}\sum_{i,\sigma,\sigma'} c_{\alpha i\sigma}^{\dagger} \boldsymbol{\sigma}_{\sigma\sigma'} c_{\alpha i\sigma'} \cdot \boldsymbol{S}_{\alpha i}. \tag{A1}$$

Here, $c_{\alpha i\sigma}^{\dagger}$ ($c_{\alpha i\sigma}$) is a creation (annihilation) operator of an itinerant electron with spin σ at site i on sublattice $\alpha = \mathrm{A}, \mathrm{B}$, and $\boldsymbol{S}_{\alpha i}$ is a classical spin ($|\boldsymbol{S}_{\alpha i}| = 1$) at site i on sublattice α. The first term represents the electron hopping. The second term represents the spin-charge coupling between the itinerant electron spin and localized spin at the same site, where $\boldsymbol{\sigma}_{\sigma\sigma'} = (\sigma^x, \sigma^y, \sigma^z)_{\sigma\sigma'}$ is a vector of the Pauli matrices. We rewrite the model in Eq. (A1) in momentum space as

$$\mathcal{H}^{\mathrm{KLM}} = \sum_{\alpha,\beta}\sum_{\boldsymbol{k},\sigma} \epsilon_{\boldsymbol{k}}^{\alpha\beta} c_{\alpha\boldsymbol{k}\sigma}^{\dagger} c_{\beta\boldsymbol{k}\sigma} + \frac{J_{\mathrm{K}}}{\sqrt{N}} \sum_{\alpha}\sum_{\boldsymbol{k},\boldsymbol{q},\sigma,\sigma'} c_{\alpha\boldsymbol{k}\sigma}^{\dagger} \boldsymbol{\sigma}_{\sigma\sigma'} c_{\alpha\boldsymbol{k}+\boldsymbol{q}\sigma'} \cdot \boldsymbol{S}_{\alpha\boldsymbol{q}}. \tag{A2}$$

Here, $\epsilon_{\boldsymbol{k}}^{\alpha\beta} = -\sum_i t_{i0}^{\alpha\beta} e^{-i\boldsymbol{k}\cdot(\boldsymbol{R}_{\alpha i}-\boldsymbol{R}_{\beta 0})} = (\epsilon_{\boldsymbol{k}}^{\beta\alpha})^*$ and N is the number of unit cells. The first term is diagonalized by the unitary matrix $U_{\boldsymbol{k}}$ as

$$\lambda_{\boldsymbol{k}}^{a} = \sum_{\alpha,\beta} \left(U_{\boldsymbol{k}}^{a\alpha}\right)^{\dagger} \epsilon_{\boldsymbol{k}}^{\alpha\beta} U_{\boldsymbol{k}}^{\beta a}, \tag{A3}$$

where $a = 1, 2$ is the band index, and

$$U_{\boldsymbol{k}} = \frac{1}{\sqrt{2}} \begin{pmatrix} 1 & \epsilon_{\boldsymbol{k}}^{\mathrm{AB}}/\left|\epsilon_{\boldsymbol{k}}^{\mathrm{AB}}\right| \\ -\epsilon_{\boldsymbol{k}}^{\mathrm{BA}}/\left|\epsilon_{\boldsymbol{k}}^{\mathrm{BA}}\right| & 1 \end{pmatrix}, \tag{A4}$$

$$\lambda_{\boldsymbol{k}}^{1} = \epsilon_{\boldsymbol{k}}^{\mathrm{AA}} - \left|\epsilon_{\boldsymbol{k}}^{\mathrm{AB}}\right|, \tag{A5}$$

$$\lambda_{\boldsymbol{k}}^{2} = \epsilon_{\boldsymbol{k}}^{\mathrm{AA}} + \left|\epsilon_{\boldsymbol{k}}^{\mathrm{AB}}\right|. \tag{A6}$$

Then, the KLM in the new basis is given by

$$\mathcal{H}^{\mathrm{KLM}} = \sum_{a}\sum_{\boldsymbol{k},\sigma} \lambda_{\boldsymbol{k}}^{a} d_{a\boldsymbol{k}\sigma}^{\dagger} d_{a\boldsymbol{k}\sigma} + \frac{J_{\mathrm{K}}}{\sqrt{N}} \sum_{a,b}\sum_{\boldsymbol{k},\boldsymbol{q},\sigma,\sigma'} d_{a\boldsymbol{k}\sigma}^{\dagger} \boldsymbol{\sigma}_{\sigma\sigma'} d_{b\boldsymbol{k}+\boldsymbol{q}\sigma'} \cdot \times \sum_{\alpha} \left(U_{\boldsymbol{k}}^{a\alpha}\right)^{\dagger} \boldsymbol{S}_{\alpha\boldsymbol{q}} U_{\boldsymbol{k}+\boldsymbol{q}}^{\alpha b}, \tag{A7}$$

where $d_{a\boldsymbol{k}\sigma}^{\dagger} = \sum_{\alpha} c_{\alpha\boldsymbol{k}\sigma}^{\dagger} U_{\boldsymbol{k}}^{\alpha a}$ and $d_{a\boldsymbol{k}\sigma} = \sum_{\alpha} (U_{\boldsymbol{k}}^{a\alpha})^{\dagger} c_{\alpha\boldsymbol{k}\sigma}$.

In Eq. (A7), we regard the second term ($\mathcal{H}'$) as the perturbation to the first term by assuming small J_{K}. When expanding the free energy with respect to $\mathcal{H}'$, the second- and fourth-order contributions are given by

$$F^{(2)} = -\frac{T}{2!}\int_0^{1/T} d\tau_1 \int_0^{1/T} d\tau_2 \langle \mathcal{T}\mathcal{H}'(\tau_1)\mathcal{H}'(\tau_2)\rangle_{\mathrm{con}}, \tag{A8}$$

$$F^{(4)} = -\frac{T}{4!}\int_0^{1/T} d\tau_1 \int_0^{1/T} d\tau_2 \int_0^{1/T} d\tau_3 \int_0^{1/T} d\tau_4 \times \langle \mathcal{T}\mathcal{H}'(\tau_1)\mathcal{H}'(\tau_2)\mathcal{H}'(\tau_3)\mathcal{H}'(\tau_4)\rangle_{\mathrm{con}}, \tag{A9}$$

respectively. Here, T is temperature, τ is the imaginary time, $\mathcal{T}$ is the time-ordered product, and $\langle\cdots\rangle_{\mathrm{con}}$ means the average over the connected Feynman diagrams. After taking the average over the connected Feynman diagrams and calculating the integral, they are written as

$$F^{(2)} = T\frac{J_{\mathrm{K}}^2}{N} \sum_{\boldsymbol{q}} \sum_{\alpha,\beta=\mathrm{A,B}} \sum_{\mu=x,y,z} \sum_{\boldsymbol{k},\omega} F_{\boldsymbol{k}}^{\beta\alpha} S_{\alpha\boldsymbol{q}}^{\mu} F_{\boldsymbol{k}+\boldsymbol{q}}^{\alpha\beta} S_{\beta-\boldsymbol{q}}^{\mu}, \tag{A10}$$

$$F^{(4)} = \frac{T}{2}\frac{J_{\mathrm{K}}^4}{N^2} \sum_{\boldsymbol{q}_1,\boldsymbol{q}_2,\boldsymbol{q}_3,\boldsymbol{q}_4} \sum_{\alpha,\beta,\gamma,\eta=\mathrm{A,B}} \sum_{\mu,\nu,\xi,\rho=x,y,z} \sum_{\boldsymbol{k},\omega} \times \delta_{\boldsymbol{q}_1+\boldsymbol{q}_2+\boldsymbol{q}_3+\boldsymbol{q}_4,\boldsymbol{0}} (\delta_{\mu,\nu}\delta_{\xi,\rho} - \delta_{\mu,\xi}\delta_{\nu,\rho} + \delta_{\rho,\mu}\delta_{\nu,\xi}) \times F_{\boldsymbol{k}}^{\eta\alpha} S_{\alpha\boldsymbol{q}_1}^{\mu} F_{\boldsymbol{k}+\boldsymbol{q}_1}^{\alpha\beta} S_{\beta\boldsymbol{q}_2}^{\nu} F_{\boldsymbol{k}+\boldsymbol{q}_1+\boldsymbol{q}_2}^{\beta\gamma} S_{\gamma\boldsymbol{q}_3}^{\xi} F_{\boldsymbol{k}+\boldsymbol{q}_1+\boldsymbol{q}_2+\boldsymbol{q}_3}^{\gamma\eta} S_{\eta\boldsymbol{q}_4}^{\rho}, \tag{A11}$$

with

$$F_{\boldsymbol{k}} = U_{\boldsymbol{k}} \begin{pmatrix} G_{1\boldsymbol{k}}(i\omega) & 0 \\ 0 & G_{2\boldsymbol{k}}(i\omega) \end{pmatrix} U_{\boldsymbol{k}}^{\dagger}, \tag{A12}$$

where $G_{a\boldsymbol{k}}(i\omega) = 1/(i\omega - \lambda_{\boldsymbol{k}}^{a} + \mu)$ is the noninteracting Green's function, ω is the Matsubara frequency, and μ is the chemical potential. As shown in the following, the RKKY (biquadratic) interaction in Eq. (1) is obtained from $F^{(2)}$ [$F^{(4)}$].

From the second-order contributions, we obtain the RKKY interaction as

$$F^{(2)} = -J_{\mathrm{K}}^2 \sum_{\boldsymbol{q}}\sum_{\alpha,\beta} \tilde{X}_{\boldsymbol{q}}^{\alpha\beta} \boldsymbol{S}_{\alpha\boldsymbol{q}} \cdot \boldsymbol{S}_{\beta-\boldsymbol{q}}, \tag{A13}$$

where

$$\tilde{X}_{\boldsymbol{q}}^{\mathrm{AA}} = \tilde{X}_{\boldsymbol{q}}^{\mathrm{BB}} = \frac{1}{4}\sum_{\boldsymbol{k}} \left(\chi_{\boldsymbol{k}\boldsymbol{q}}^{11} + \chi_{\boldsymbol{k}\boldsymbol{q}}^{22} + \chi_{\boldsymbol{k}\boldsymbol{q}}^{12} + \chi_{\boldsymbol{k}\boldsymbol{q}}^{21}\right), \tag{A14}$$

$$\tilde{X}_{\boldsymbol{q}}^{\mathrm{AB}} = \left(\tilde{X}_{\boldsymbol{q}}^{\mathrm{BA}}\right)^* = \frac{1}{4}\sum_{\boldsymbol{k}} \frac{\epsilon_{\boldsymbol{k}+\boldsymbol{q}}^{\mathrm{AB}}}{\left|\epsilon_{\boldsymbol{k}+\boldsymbol{q}}^{\mathrm{AB}}\right|} \frac{\left(\epsilon_{\boldsymbol{k}}^{\mathrm{AB}}\right)^*}{\left|\epsilon_{\boldsymbol{k}}^{\mathrm{AB}}\right|} \left(\chi_{\boldsymbol{k}\boldsymbol{q}}^{11} + \chi_{\boldsymbol{k}\boldsymbol{q}}^{22} - \chi_{\boldsymbol{k}\boldsymbol{q}}^{12} - \chi_{\boldsymbol{k}\boldsymbol{q}}^{21}\right), \tag{A15}$$

$$\chi_{\boldsymbol{k}\boldsymbol{q}}^{ab} = -\sum_{\omega} \frac{T}{N} G_{a\boldsymbol{k}}(i\omega) G_{b\boldsymbol{k}+\boldsymbol{q}}(i\omega) = \frac{1}{N}\frac{f(\lambda_{a\boldsymbol{k}}) - f(\lambda_{b\boldsymbol{k}+\boldsymbol{q}})}{\lambda_{b\boldsymbol{k}+\boldsymbol{q}} - \lambda_{a\boldsymbol{k}}} > 0. \tag{A16}$$

In the main text, we set $JX^{\mathrm{AA}} = J_{\mathrm{K}}^2 \tilde{X}_{\boldsymbol{Q}_\eta}^{\mathrm{AA}} = \cos^2\Theta$ and $JX^{\mathrm{AB}} = J_{\mathrm{K}}^2 \tilde{X}_{\boldsymbol{Q}_\eta}^{\mathrm{AB}} = \pm\sin^2\Theta$ with $0 < \Theta \leqslant \pi/2$. According to Eqs. (A14) and (A15), $\tilde{X}_{\boldsymbol{q}}^{\mathrm{AA}}$ is positive and larger than

$|\tilde{X}^{\rm AB}_{\boldsymbol{q}}|$. Thus, the region for $0 < \Theta < \pi/4$ is connected to the honeycomb KLM in Eq. (A1), while that for $\Theta \geqslant \pi/4$ is described by additionally introducing the direct exchange interaction between sublattices A and B, which can modulate $X^{\rm AB}$ so as to be larger than $X^{\rm AA}$ effectively.

Among the fourth-order contributions, we focus on the biquadratic interactions with the form of $(\boldsymbol{S}_{\alpha\boldsymbol{q}} \cdot \boldsymbol{S}_{\beta-\boldsymbol{q}})(\boldsymbol{S}_{\gamma\boldsymbol{q}} \cdot \boldsymbol{S}_{\eta-\boldsymbol{q}})$ in the main text by supposing the strong nesting property at a particular set of $\boldsymbol{q}$. Then, the fourth-order term in Eq. (A11) is explicitly written down as

$$F_1^{(4)} = 2\frac{J_{\rm K}^4}{N} C_1^{\rm AAAA}[(\boldsymbol{S}_{{\rm A}\boldsymbol{q}} \cdot \boldsymbol{S}_{{\rm A}-\boldsymbol{q}})^2 + (\boldsymbol{S}_{{\rm B}\boldsymbol{q}} \cdot \boldsymbol{S}_{{\rm B}-\boldsymbol{q}})^2], \quad \text{(A17)}$$

$$F_2^{(4)} = 2\frac{J_{\rm K}^4}{N} C_1^{\rm BABA}(\boldsymbol{S}_{{\rm A}\boldsymbol{q}} \cdot \boldsymbol{S}_{{\rm B}-\boldsymbol{q}})^2, \quad \text{(A18)}$$

$$F_3^{(4)} = 2\frac{J_{\rm K}^4}{N} C_1^{\rm ABAB}(\boldsymbol{S}_{{\rm B}\boldsymbol{q}} \cdot \boldsymbol{S}_{{\rm A}-\boldsymbol{q}})^2, \quad \text{(A19)}$$

$$F_4^{(4)} = 2\frac{J_{\rm K}^4}{N}\big(C_1^{\rm AABB} + C_1^{\rm BAAB} + 2C_2^{\rm AABB} - C_2^{\rm BABA} - C_2^{\rm ABAB}\big)(\boldsymbol{S}_{{\rm A}\boldsymbol{q}} \cdot \boldsymbol{S}_{{\rm A}-\boldsymbol{q}})(\boldsymbol{S}_{{\rm B}\boldsymbol{q}} \cdot \boldsymbol{S}_{{\rm B}-\boldsymbol{q}}), \quad \text{(A20)}$$

$$F_5^{(4)} = 4\frac{J_{\rm K}^4}{N} C_1^{\rm AABA}[(\boldsymbol{S}_{{\rm A}\boldsymbol{q}} \cdot \boldsymbol{S}_{{\rm A}-\boldsymbol{q}})(\boldsymbol{S}_{{\rm A}\boldsymbol{q}} \cdot \boldsymbol{S}_{{\rm B}-\boldsymbol{q}}) + (\boldsymbol{S}_{{\rm B}\boldsymbol{q}} \cdot \boldsymbol{S}_{{\rm B}-\boldsymbol{q}})(\boldsymbol{S}_{{\rm A}\boldsymbol{q}} \cdot \boldsymbol{S}_{{\rm B}-\boldsymbol{q}})], \quad \text{(A21)}$$

$$F_6^{(4)} = 4\frac{J_{\rm K}^4}{N} C_1^{\rm AAAB}[(\boldsymbol{S}_{{\rm A}\boldsymbol{q}} \cdot \boldsymbol{S}_{{\rm A}-\boldsymbol{q}})(\boldsymbol{S}_{{\rm B}\boldsymbol{q}} \cdot \boldsymbol{S}_{{\rm A}-\boldsymbol{q}}) + (\boldsymbol{S}_{{\rm B}\boldsymbol{q}} \cdot \boldsymbol{S}_{{\rm B}-\boldsymbol{q}})(\boldsymbol{S}_{{\rm A}\boldsymbol{q}} \cdot \boldsymbol{S}_{{\rm A}-\boldsymbol{q}})], \quad \text{(A22)}$$

$$F_7^{(4)} = 2\frac{J_{\rm K}^4}{N}\big(C_1^{\rm AABB} + C_1^{\rm BAAB} - 2C_2^{\rm AABB} + C_2^{\rm BABA} + C_2^{\rm ABAB}\big)(\boldsymbol{S}_{{\rm A}\boldsymbol{q}} \cdot \boldsymbol{S}_{{\rm B}-\boldsymbol{q}})(\boldsymbol{S}_{{\rm B}\boldsymbol{q}} \cdot \boldsymbol{S}_{{\rm A}-\boldsymbol{q}}), \quad \text{(A23)}$$

where

$$C_1^{\alpha\beta\gamma\eta} = \frac{T}{N}\sum_{\boldsymbol{k},\omega} F_{\boldsymbol{k}}^{\alpha\beta} F_{\boldsymbol{k}+\boldsymbol{q}}^{\beta\gamma} F_{\boldsymbol{k}}^{\gamma\eta} F_{\boldsymbol{k}+\boldsymbol{q}}^{\eta\alpha}, \quad \text{(A24)}$$

$$C_2^{\alpha\beta\gamma\eta} = \frac{T}{N}\sum_{\boldsymbol{k},\omega} F_{\boldsymbol{k}}^{\alpha\beta} F_{\boldsymbol{k}+\boldsymbol{q}}^{\beta\gamma} F_{\boldsymbol{k}+2\boldsymbol{q}}^{\gamma\eta} F_{\boldsymbol{k}+\boldsymbol{q}}^{\eta\alpha}. \quad \text{(A25)}$$

In the main text, we simplify $C_1^{\alpha\beta\gamma\eta}$ and $C_2^{\alpha\beta\gamma\eta}$ as follows:

$$K(X^{\rm AA})^2 = 2J_{\rm K}^4 C_1^{\rm AAAA} = 2J_{\rm K}^4\big(C_1^{\rm AABB} + C_1^{\rm BAAB} + 2C_2^{\rm AABB} - C_2^{\rm BABA} - C_2^{\rm ABAB}\big), \quad \text{(A26)}$$

$$K(X^{\rm AB})^2 = 2J_{\rm K}^4 C_1^{\rm BABA} = 2J_{\rm K}^4 C_1^{\rm ABAB} = 2J_{\rm K}^4\big(C_1^{\rm AABB} + C_1^{\rm BAAB} - 2C_2^{\rm AABB} + C_2^{\rm BABA} + C_2^{\rm ABAB}\big), \quad \text{(A27)}$$

$$KX^{\rm AA}X^{\rm AB} = 4J_{\rm K}^4 C_1^{\rm AABA} = 4J_{\rm K}^4 C_1^{\rm AAAB}. \quad \text{(A28)}$$

The other cases with different sets of $C_1^{\alpha\beta\gamma\eta}$ and $C_2^{\alpha\beta\gamma\eta}$ are left for future studies.

TABLE I. Critical magnetic fields $H_{\rm c1}$, $H_{\rm c2}$, $H_{\rm c3}$, and $H_{\rm c4}$ for multiple topological transitions at specific Θ. Here, we find AFC SkX II at $0 \leqslant H < H_{\rm c1}$, the FerriC SkX at $H_{\rm c1} < H < H_{\rm c2}$, AFC SkX I at $H_{\rm c2} < H < H_{\rm c3}$, and the FC SkX I at $H_{\rm c3} < H < H_{\rm c4}$.

	Θ	$H_{\rm c1}$	$H_{\rm c2}$	$H_{\rm c3}$	$H_{\rm c4}$
Case (i)	$5\pi/48$	0.3875	0.4125	0.4825	0.8625
Case (ii)	$\pi/6$	0.2625	0.3375	0.4625	0.9125
Case (iii)	$7\pi/48$	0.3375	0.3625	0.5375	0.9625

APPENDIX B: SKYRMION CRYSTALS IN THE MODELS WITH DIFFERENT FORM FACTORS

We consider the effective spin model with different form factors for the RKKY and biquadratic interactions, which is given by

$$\mathcal{H}^{\rm eff} = -2J\sum_{\eta}\sum_{\alpha,\beta} X^{\alpha\beta}\boldsymbol{S}_{\alpha\boldsymbol{Q}_\eta} \cdot \boldsymbol{S}_{\beta-\boldsymbol{Q}_\eta} + 2\frac{K}{N}\sum_{\eta}\left(\sum_{\alpha,\beta} X_{\rm K}^{\alpha\beta}\boldsymbol{S}_{\alpha\boldsymbol{Q}_\eta} \cdot \boldsymbol{S}_{\beta-\boldsymbol{Q}_\eta}\right)^2 - H\sum_{\alpha,i} S_{\alpha i}^z. \quad \text{(B1)}$$

Here, $X^{\alpha\beta}$ and $X_{\rm K}^{\alpha\beta}$ are the form factors for the RKKY interaction and biquadratic interaction, respectively. Although we consider the case of $X^{\alpha\beta} = X_{\rm K}^{\alpha\beta}$ in the main text for simplicity, the form factors are usually different. In this section, we show that the SkX phases in Fig. 3 also appear even for $X^{\alpha\beta} \neq X_{\rm K}^{\alpha\beta}$. Specifically, we consider three different $X_{\rm K}^{\alpha\beta}$ while fixing $X^{\rm AA} \equiv \cos^2\Theta$ and $X^{\rm AB} \equiv -\sin^2\Theta$ to cover various situations: (i) $X_{\rm K}^{\rm AA} \equiv \cos^2\Theta$ and $X_{\rm K}^{\rm AB} \equiv \sin^2\Theta$, (ii) $X_{\rm K}^{\rm AA} \equiv \sin^2\Theta$ and $X_{\rm K}^{\rm AB} \equiv -\cos^2\Theta$, and (iii) $X_{\rm K}^{\rm AA} \equiv \sin^2\Theta$ and $X_{\rm K}^{\rm AB} \equiv \cos^2\Theta$. By following the same manner of the simulation in the main text, we find FC SkX I, AFC SkXs I and II, and FerriC SkX in various Θ and H. For example, we show critical magnetic fields for multiple topological transitions at $K = 0.4$ in Table I, where AFC SkX II appears at low fields including $H = 0$, FerriC SkX appears above $H_{\rm c1}$, AFC SkX I appears above $H_{\rm c2}$, FC SkX I appears above $H_{\rm c3}$, and other trivial states appear above $H_{\rm c4}$ while increasing H. In this way, a variety of SkXs discussed in the main text are ubiquitously stabilized in the effective spin model with the antiferromagnetic intersublattice RKKY interaction and the positive biquadratic interaction irrespective of the form factor $X_{\rm K}^{\alpha\beta}$.

APPENDIX C: ANALYTICAL CALCULATION AT ZERO FIELD

We discuss the instability toward the CS and SkX states in the ground states at zero field in Fig. 2(a) in the main text by using analytical variational calculations. We consider the model in Eq. (1) with $X^{\rm AA} = X^{\rm BB} = \cos^2\Theta$ and $X^{\rm AB} = X^{\rm BA} = \sigma\sin^2\Theta$ ($\sigma = \pm 1$). Variational states for each σ are two types of single-Q ($1Q$) spiral states, two types of CS states, and SkX II. After giving the variational states and

calculating their energies, we discuss the instability toward the CS and SkX states from the $1Q$ spiral states.

1. Single-Q spiral state

We define $1Q$ spiral I and II states as the variational states and calculate their energies. The $1Q$ spiral I state is defined by

$$\boldsymbol{S}_{\mathrm{A}i}^{1Q\mathrm{I}} = \boldsymbol{e}_x \cos \mathcal{Q}_{\mathrm{A}i}^1 - \boldsymbol{e}_y \sin \mathcal{Q}_{\mathrm{A}i}^1, \tag{C1}$$

$$\boldsymbol{S}_{\mathrm{B}i}^{1Q\mathrm{I}} = \boldsymbol{e}_x \cos \mathcal{Q}_{\mathrm{B}i}^2 - \boldsymbol{e}_y \sin \mathcal{Q}_{\mathrm{B}i}^2, \tag{C2}$$

where $\mathcal{Q}_{\alpha i}^{\eta} = \boldsymbol{Q}_{\eta} \cdot \boldsymbol{R}_{\alpha i}$ and $\boldsymbol{e}_{\mu}$ is the unit vector along the $\mu = x, y, z$ direction. In this state, the ordering wave vector for sublattice A is different from that for sublattice B. Their spiral planes are arbitrary due to continuous rotational symmetry in spin space and are independent of each other. The energy per unit cell is given by

$$E^{1Q\mathrm{I}} = -2JX^{\mathrm{AA}} + K(X^{\mathrm{AA}})^2. \tag{C3}$$

The $1Q$ spiral II state is defined by

$$\boldsymbol{S}_{\mathrm{A}i}^{1Q\mathrm{II}} = \boldsymbol{e}_x \cos \mathcal{Q}_{\mathrm{A}i}^1 - \boldsymbol{e}_y \sin \mathcal{Q}_{\mathrm{A}i}^1, \tag{C4}$$

$$\boldsymbol{S}_{\mathrm{B}i}^{1Q\mathrm{II}} = \boldsymbol{e}_x \cos\left(\mathcal{Q}_{\mathrm{B}i}^1 + \Delta\right) - (\boldsymbol{e}_y \cos\theta + \boldsymbol{e}_z \sin\theta) \sin\left(\mathcal{Q}_{\mathrm{B}i}^1 + \Delta\right), \tag{C5}$$

where Δ and θ are variational parameters. The energy per unit cell is given by

$$E^{1Q\mathrm{II}}(\Delta,\theta) = -2J\left(X^{\mathrm{AA}} + X^{\mathrm{AB}} \cos^2\frac{\theta}{2} \cos\Delta\right) + 2K\left(X^{\mathrm{AA}} + X^{\mathrm{AB}} \cos^2\frac{\theta}{2} \cos\Delta\right)^2. \tag{C6}$$

For $\sigma = +1$ $(\sigma = -1)$ and $K/J < 0.5$, $E^{1Q\mathrm{II}}(\Delta,\theta)$ has the minimum energy at $\Delta = 0$ $(\Delta = \pi)$ and $\theta = 0$. Then, the minimum energy is given by $E^{1Q\mathrm{II}} = -2J + 2K$. Thus, the ordering wave vectors and spiral planes are the same between the sublattices and the spins at $\boldsymbol{R}_{\mathrm{A}i}$ and $\boldsymbol{R}_{\mathrm{B}i} = \boldsymbol{R}_{\mathrm{A}i} + \boldsymbol{d}_{\eta}^*$ are parallel (antiparallel) in the $1Q$ spiral II state, where $\boldsymbol{d}_{\eta}^*$ is the displacement vector for three nearest-neighbor bonds shown in the inset of Fig. 2(a) in the main text.

2. Chiral stripe state

We consider the energies for the CS I and II states, which are obtained by numerical calculations in Fig. 2(a) in the main text. The CS I state for the model with $\sigma = \pm 1$ is expressed as the superposition of the $1Q$ spiral I and sinusoidal waves, whose spin configuration is given by

$$\boldsymbol{S}_{\mathrm{A}i}^{\mathrm{CSI}} = \sqrt{1 - b^2 \sin^2 \mathcal{Q}_{\mathrm{A}i}^3}\left(\boldsymbol{e}_x \cos \mathcal{Q}_{\mathrm{A}i}^1 - \boldsymbol{e}_y \sin \mathcal{Q}_{\mathrm{A}i}^1\right) + \boldsymbol{e}_z b \sin \mathcal{Q}_{\mathrm{A}i}^3, \tag{C7}$$

$$\boldsymbol{S}_{\mathrm{B}i}^{\mathrm{CSI}} = \sqrt{1 - b^2 \sin^2 \mathcal{Q}_{\mathrm{B}i}^3}\left(\boldsymbol{e}_x \cos \mathcal{Q}_{\mathrm{B}i}^2 - \boldsymbol{e}_y \sin \mathcal{Q}_{\mathrm{B}i}^2\right) + \boldsymbol{e}_z \sigma b \sin \mathcal{Q}_{\mathrm{B}i}^3, \tag{C8}$$

where the variational parameter b $(0 < b < 1)$ represents the amplitude of the sinusoidal wave [23,47]. In this state, the ordering wave vectors for the spiral (sinusoidal) wave are different (the same) between the sublattices; the sinusoidal wave oscillates along the direction perpendicular to the spiral plane. It is noted that the CS I state is continuously connected to the $1Q$ spiral I state by $b \to 0$. To calculate the energy, we use the following Fourier transform of the CS I spin configuration:

$$\boldsymbol{S}_{\mathrm{A}\boldsymbol{Q}_1}^{\mathrm{CSI}} = \frac{\sqrt{N}}{2} C_0(\boldsymbol{e}_x - i\boldsymbol{e}_y), \tag{C9}$$

$$\boldsymbol{S}_{\mathrm{A}\boldsymbol{Q}_3}^{\mathrm{CSI}} = i\frac{\sqrt{N}}{2} b\boldsymbol{e}_z, \tag{C10}$$

$$\boldsymbol{S}_{\mathrm{B}\boldsymbol{Q}_2}^{\mathrm{CSI}} = \frac{\sqrt{N}}{2} C_0(\boldsymbol{e}_x - i\boldsymbol{e}_y), \tag{C11}$$

$$\boldsymbol{S}_{\mathrm{B}\boldsymbol{Q}_3}^{\mathrm{CSI}} = i\frac{\sqrt{N}}{2} \sigma b\boldsymbol{e}_z, \tag{C12}$$

where N is the number of unit cells and $C_0 = 1 - b^2/4 - 3b^4/64 + \mathcal{O}(b^6)$. The energy per unit cell is

$$\begin{aligned} E^{\mathrm{CSI}}(b) &= -2J\left[X^{\mathrm{AA}} C_0^2 + \frac{b^2}{2}(X^{\mathrm{AA}} + \sigma X^{\mathrm{AB}})\right] \\ &\quad + 2K\left[\frac{1}{2}(X^{\mathrm{AA}})^2 C_0^4 + \frac{b^4}{4}(X^{\mathrm{AA}} + \sigma X^{\mathrm{AB}})^2\right], \\ &= -2J\left[X^{\mathrm{AA}}\left(1 - \frac{b^2}{2} - \frac{b^4}{32}\right) + \frac{b^2}{2}\right] \\ &\quad + K\left[(X^{\mathrm{AA}})^2\left(1 - b^2 + \frac{3}{16}b^4\right) + \frac{b^4}{2}\right] + \mathcal{O}(b^6), \end{aligned} \tag{C13}$$

where we use $X^{\mathrm{AA}} + \sigma X^{\mathrm{AB}} = 1$.

Next, we consider the energy for the CS II state. By introducing the sinusoidal-wave modulation to the $1Q$ spiral II state, we describe the CS II state for the model with $\sigma = \pm 1$ as

$$\boldsymbol{S}_{\mathrm{A}i}^{\mathrm{CSII}} = \sqrt{1 - b^2 \sin^2 \mathcal{Q}_{\mathrm{A}i}^2}\left(\boldsymbol{e}_x \cos \mathcal{Q}_{\mathrm{A}i}^1 - \boldsymbol{e}_y \sin \mathcal{Q}_{\mathrm{A}i}^1\right) + \boldsymbol{e}_z b \sin \mathcal{Q}_{\mathrm{A}i}^2, \tag{C14}$$

$$\boldsymbol{S}_{\mathrm{B}i}^{\mathrm{CSII}} = \sigma\sqrt{1 - b^2 \sin^2 \mathcal{Q}_{\mathrm{B}i}^2}\left(\boldsymbol{e}_x \cos \mathcal{Q}_{\mathrm{B}i}^1 - \boldsymbol{e}_y \sin \mathcal{Q}_{\mathrm{B}i}^1\right) + \boldsymbol{e}_z \sigma b \sin \mathcal{Q}_{\mathrm{B}i}^2, \tag{C15}$$

with $0 < b < 1$. In this state, the ordering wave vectors for the spiral (sinusoidal) wave, the spiral planes, and the oscillation directions of the sinusoidal wave are the same between the sublattices. As well as the CS I state, the sinusoidal wave oscillates along the direction perpendicular to the spiral plane and the CS II state is continuously connected to the $1Q$ spiral II state by $b \to 0$. The energy per unit cell is

$$E^{\mathrm{CSII}}(b) = -2J(X^{\mathrm{AA}} + \sigma X^{\mathrm{AB}})\left(C_0^2 + \frac{b^2}{2}\right) + 2K(X^{\mathrm{AA}} + \sigma X^{\mathrm{AB}})^2\left(C_0^4 + \frac{b^2}{4}\right)$$

$$= -2J\left(1 - \frac{b^4}{32}\right) + 2K\left(1 - b^2 + \frac{7}{16}b^4\right) + \mathcal{O}(b^6). \quad \text{(C16)}$$

3. Skyrmion crystal II state

The SkX II for the model with $\sigma = \pm 1$, which also appears in Fig. 2(a) in the main text, is expressed as the superposition of three sinusoidal waves as

$$\boldsymbol{S}_{\mathrm{A}i}^{\mathrm{SkXII}} = \frac{1}{N_{\mathrm{A}i}}\left(\cos \mathcal{Q}_{\mathrm{A}i}^{1}\boldsymbol{e}_x + \cos \mathcal{Q}_{\mathrm{A}i}^{2}\boldsymbol{e}_y + \cos \mathcal{Q}_{\mathrm{A}i}^{3}\boldsymbol{e}_z\right), \quad \text{(C17)}$$

$$\boldsymbol{S}_{\mathrm{B}i}^{\mathrm{SkXII}} = \frac{\sigma}{N_{\mathrm{B}i}}\left(\cos \mathcal{Q}_{\mathrm{B}i}^{1}\boldsymbol{e}_x + \cos \mathcal{Q}_{\mathrm{B}i}^{2}\boldsymbol{e}_y + \cos \mathcal{Q}_{\mathrm{B}i}^{3}\boldsymbol{e}_z\right), \quad \text{(C18)}$$

where $N_{\alpha i} = \sqrt{\sum_{\eta=1}^{3} \cos^2 \mathcal{Q}_{\alpha i}^{\eta}}$. The SkX II with $\sigma = 1$ ($\sigma = -1$) corresponds to the FC (AFC) SkX II. We approximately give the Fourier transform of this configuration as

$$|\boldsymbol{S}_{\mathrm{A}\boldsymbol{Q}_\eta}| = |\boldsymbol{S}_{\mathrm{B}\boldsymbol{Q}_\eta}| = \sqrt{\frac{N}{6}}(1-\delta), \quad \text{(C19)}$$

where we introduce the variational parameter δ to take into account the higher harmonics of the sinusoidal wave [23]. The energy per unit cell is given by

$$\begin{aligned} E^{\mathrm{SkXII}}(\delta) &= -2J(X^{\mathrm{AA}} + |X^{\mathrm{AB}}|)(1-\delta)^2 \\ &\quad + \tfrac{2}{3}K(X^{\mathrm{AA}} + |X^{\mathrm{AB}}|)^2(1-\delta)^4 \\ &\approx -2J(X^{\mathrm{AA}} + |X^{\mathrm{AB}}|)(1-2\delta) \\ &\quad + \tfrac{2}{3}K(X^{\mathrm{AA}} + |X^{\mathrm{AB}}|)^2(1-4\delta) \\ &= -2J(1-2\delta) + \tfrac{2}{3}K(1-4\delta). \end{aligned} \quad \text{(C20)}$$

4. Energy comparison

We discuss the instability toward the CS and SkX states from the $1Q$ spiral state. The model in Eq. (1) has three parameters σ (sign of X^{AB}), Θ, and K/J at zero field, while the energies in Eqs. (C3), (C6), (C13), (C16), and (C20) do not depend on σ. In other words, the phase boundary in Fig. 2(a) is irrespective of σ, as discussed in the main text. Therefore, we focus on Θ and K/J dependencies of the energy in the following. First, we identify a parameter region I (II) where the $1Q$ spiral I (II) state is more stable than the $1Q$ spiral II (I) state. By solving $E^{1QI} - E^{1QII} = 0$ with respect to K, we obtain

$$\frac{K_c(\Theta)}{J} = \frac{2(1-X^{\mathrm{AA}})}{2-(X^{\mathrm{AA}})^2} = \frac{2\sin^2\Theta}{2-\cos^4\Theta}. \quad \text{(C21)}$$

Then, region I (II) is defined by $K > K_c(\Theta)$ [$K < K_c(\Theta)$]. We show $K_c(\Theta)$ with the solid line in Fig. 4(a), where the $K_c(\Theta)$ curve is qualitatively consistent with the phase boundary between the CS I and II phases. This is because the CS I (II) state is continuously connected to the $1Q$ spiral I (II) state. Furthermore, this result means that the spiral state at $K = 0$ in Fig. 4(a) is the $1Q$ spiral II state. Figure 4(a) shows that the CS I (II) and SkX II states have lower energy than the $1Q$ spiral I (II) state in region I (II) at $K \neq 0$, which we will confirm by variational calculations in the following.

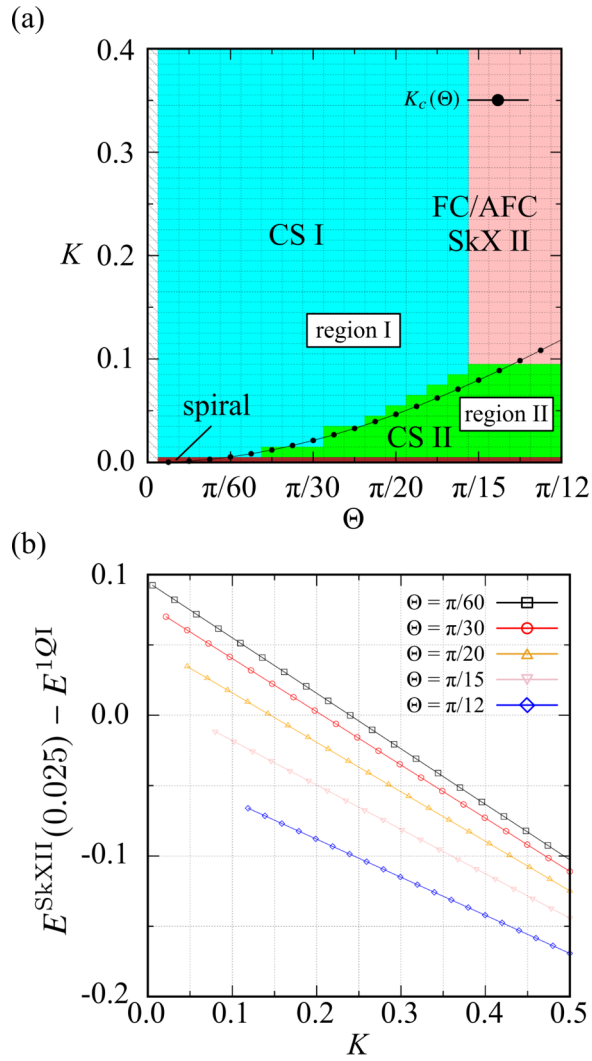

FIG. 4. (a) Phase diagram at zero field with $K_c(\Theta)$. The $K_c(\Theta)$ curve divides the phase diagram into regions I and II. (b) K dependence of the energy difference between the SkX II and $1Q$ spiral I states for $\Theta = \pi/60$ (black), $\Theta = \pi/30$ (red), $\Theta = \pi/20$ (orange), $\Theta = \pi/15$ (pink), and $\Theta = \pi/12$ (blue), where we set $\delta = 0.025$ based on the simulation results. We plot the data in region I, i.e., $K > K_c(\Theta)$.

a. Region I

The energy difference between the CS I and $1Q$ spiral I states is given by

$$E^{\mathrm{CSI}}(b) - E^{1QI} = -b^2[J(1-X^{\mathrm{AA}}) + K(X^{\mathrm{AA}})^2] + \frac{b^4}{16}[JX^{\mathrm{AA}} + 3K(X^{\mathrm{AA}})^2 + 8K]. \quad \text{(C22)}$$

The energy difference becomes negative when

$$\begin{aligned} 0 < b^2 &< 16\frac{J(1-X^{\mathrm{AA}}) + K(X^{\mathrm{AA}})^2}{JX^{\mathrm{AA}} + 3K(X^{\mathrm{AA}})^2 + 8K} \\ &= 16\frac{J\sin^2\Theta + K\cos^4\Theta}{J\cos^2\Theta + 3K\cos^4\Theta + 8K}, \end{aligned} \quad \text{(C23)}$$

which means that the CS I state with infinitesimal b is more stable than the $1Q$ spiral I state in region I. This result is

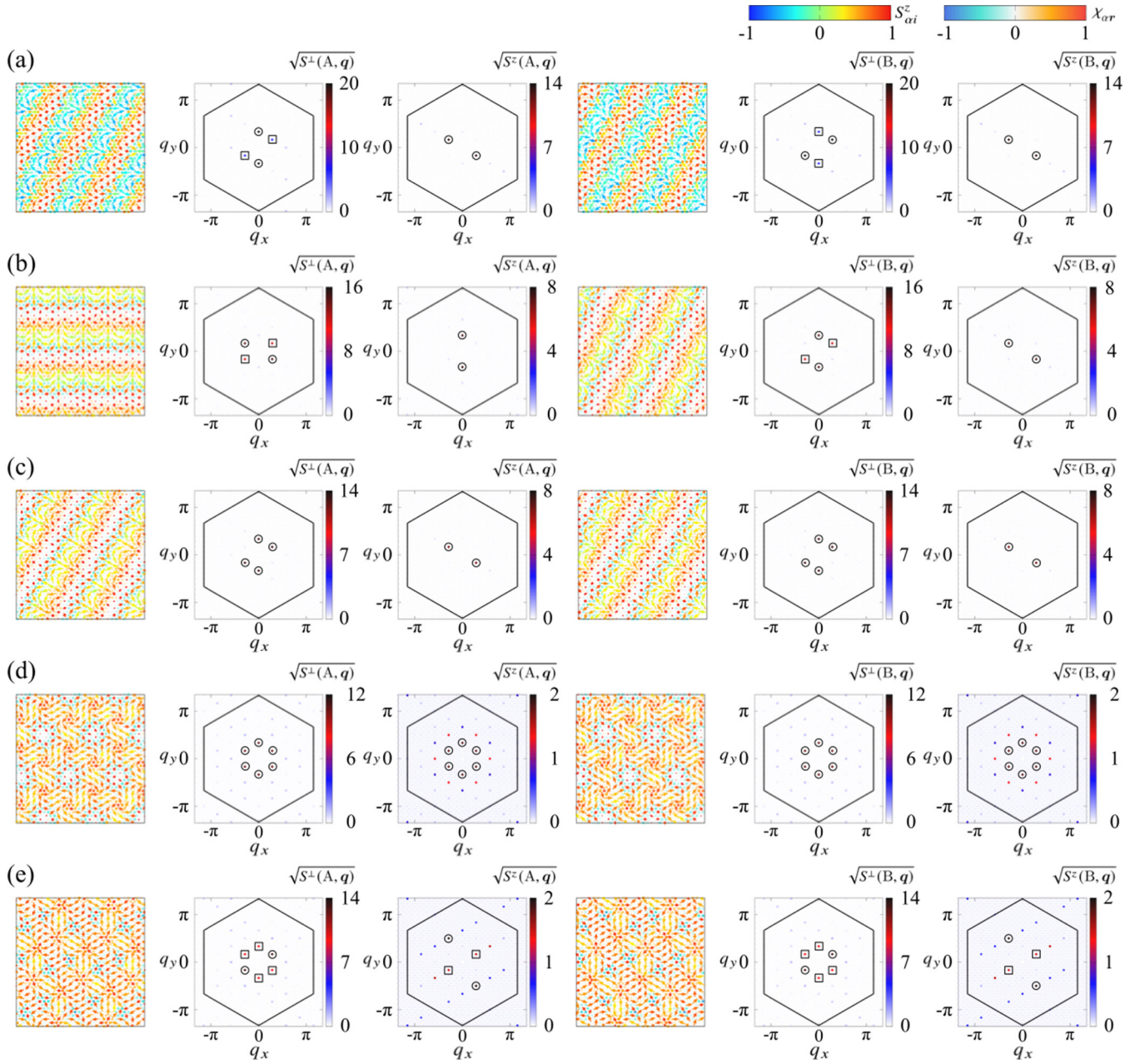

FIG. 5. First (fourth) column: Spin ($\boldsymbol{S}_{\alpha i}$) and chirality ($\chi_{\alpha r}$) configurations on sublattice A (B) of (a) the trivial state I at $\Theta = \pi/24$ and $H = 0.3$, (b) the trivial state II at $\Theta = \pi/24$ and $H = 1$, (c) the trivial state III at $\Theta = 5\pi/48$ and $H = 1$, (d) the trivial state IV at $\Theta = \pi/6$ and $H = 1$, and (e) the trivial state V at $\Theta = \pi/4$ and $H = 1$. The arrows, contours of arrows, and contours of circles show the xy spin component, z spin component, and spin scalar chirality, respectively. Second and third (fifth and sixth) columns: The in-plane $[S^\perp(\alpha, \boldsymbol{q})]$ and out-of-plane $[S^z(\alpha, \boldsymbol{q})]$ spin structure factors for sublattice A (B) in momentum space, respectively. The circle and square highlight the dominant and subdominant peaks, respectively. The hexagons with a solid line show the first Brillouin zone. The $\boldsymbol{q} = \boldsymbol{0}$ component is removed for better visibility.

consistent with the ground-state phase diagram, where the $1Q$ spiral I phase does not appear.

The energy difference between the SkX II and $1Q$ spiral I states is given by

$$E^{\mathrm{SkXII}}(\delta) - E^{1Q\mathrm{I}} = -2J[1 - 2\delta - X^{\mathrm{AA}}] + \frac{K}{3}[2 - 8\delta - 3(X^{\mathrm{AA}})^2]. \quad \text{(C24)}$$

The energy difference monotonically decreases while increasing Θ for $K/J < 1$. This behavior explains that the SkX II appears for the larger Θ region in Fig. 4(a). Figure 4(b) shows the K dependence of the energy difference for various Θ at $\delta = 0.025$, where we use a typical value of δ obtained from the numerical simulation. The result shows that the SkX II state becomes stable in a larger K region, which is consistent with the simulation results in Fig. 4(a). It is noted that the discussion based on Eq. (C24) overestimates the stability of

the SkX II state because the CS I state has a lower energy than the $1Q$ spiral I state.

b. Region II

The energy difference between the CS II and $1Q$ spiral II states is

$$E^{\mathrm{CSII}}(b) - E^{1Q\mathrm{II}} = -2b^2K + \tfrac{1}{16}b^4(J + 14K). \tag{C25}$$

The stable condition for the CS II state is

$$0 < b^2 < \frac{32K}{J + 14K}. \tag{C26}$$

This explains the behavior that the $1Q$ spiral II state at $K = 0$ changes into the CS II state by introducing an infinitesimal K in Fig. 4(a).

The energy difference between the SkX II and $1Q$ spiral II states is given by

$$E^{\mathrm{SkXII}}(\delta) - E^{1Q\mathrm{II}} = 4J\delta - \tfrac{4}{3}K(1 + 2\delta). \tag{C27}$$

The SkX II has lower energy when

$$\frac{K}{J} > \frac{3\delta}{1 + 2\delta}. \tag{C28}$$

The absence of the Θ dependence is consistent with the simulation result. Specifically, the stable condition for the SkX II state is $K/J > 0.071$ for $\delta = 0.025$, which is qualitatively consistent with the ground-state phase diagram in Fig. 4(a). Similar to the case between the $1Q$ spiral I and SkX II states, the overestimation of the stable condition might arise due to not taking into account the CS II state.

APPENDIX D: TRIVIAL PHASES I–V

In Fig. 3, we find the field-induced trivial phases denoted as I–V with $N_{\mathrm{sk}}^{\mathrm{tot}} = N_{\mathrm{sk}}^{\mathrm{stagg}} = 0$. We show their spin configurations, chirality configurations, and spin structure factors in Fig. 5. Since all the phases exhibit the triple-Q peaks at $\boldsymbol{Q}_1 = (0, \pi/3)$, $\boldsymbol{Q}_2 = (-\sqrt{3}\pi/6, -\pi/6)$, and $\boldsymbol{Q}_3 = (\sqrt{3}\pi/6, -\pi/6)$ in the spin structure factor, they are regarded as triple-Q states. The trivial spin configurations I and II are characterized by the double-Q in-plane spin structure factor and the single-Q out-of-plane one, as shown in Figs. 5(a) and 5(b), respectively, where the peak positions depend on the sublattices. The trivial state I is characterized by the sublattice-dependent in-plane spin structure factor and sublattice-independent out-of-plane one: $S^{\perp}(\mathrm{A}, \boldsymbol{Q}_1) > S^{\perp}(\mathrm{A}, \boldsymbol{Q}_2)$ and $S^{z}(\mathrm{A}, \boldsymbol{Q}_3)$ for sublattice A and $S^{\perp}(\mathrm{B}, \boldsymbol{Q}_2) > S^{\perp}(\mathrm{B}, \boldsymbol{Q}_1)$ and $S^{z}(\mathrm{B}, \boldsymbol{Q}_3)$ for sublattice B. The trivial phase II shows the sublattice-dependent in-plane and out-of-plane spin structure factors: $S^{\perp}(\mathrm{A}, \boldsymbol{Q}_3) > S^{\perp}(\mathrm{A}, \boldsymbol{Q}_2)$ and $S^{z}(\mathrm{A}, \boldsymbol{Q}_1)$ for sublattice A and $S^{\perp}(\mathrm{B}, \boldsymbol{Q}_1) > S^{\perp}(\mathrm{B}, \boldsymbol{Q}_2)$ and $S^{z}(\mathrm{B}, \boldsymbol{Q}_3)$ for sublattice B. Meanwhile, the trivial spin configurations III–V show the sublattice-independent in-plane and out-of-plane spin structure factors: $S^{\perp}(\alpha, \boldsymbol{Q}_1) = S^{\perp}(\alpha, \boldsymbol{Q}_2)$ and $S^{z}(\alpha, \boldsymbol{Q}_3)$ for $\alpha = \mathrm{A}, \mathrm{B}$ in phase III, $S^{\perp(z)}(\alpha, \boldsymbol{Q}_1) = S^{\perp(z)}(\alpha, \boldsymbol{Q}_2) = S^{\perp(z)}(\alpha, \boldsymbol{Q}_3)$ for $\alpha = \mathrm{A}, \mathrm{B}$ in phase IV, and $S^{\perp}(\alpha, \boldsymbol{Q}_2) > S^{\perp}(\alpha, \boldsymbol{Q}_1) = S^{\perp}(\alpha, \boldsymbol{Q}_3)$ and $S^{z}(\alpha, \boldsymbol{Q}_1 - \boldsymbol{Q}_3) > S^{z}(\alpha, \boldsymbol{Q}_2)$ for $\alpha = \mathrm{A}, \mathrm{B}$ in phase V.

[1] N. Nagaosa and Y. Tokura, Nat. Nanotechnol. **8**, 899 (2013).
[2] Y. Tokura and N. Kanazawa, Chem. Rev. **121**, 2857 (2021).
[3] X. Zhang, Y. Zhou, K. M. Song, T.-E. Park, J. Xia, M. Ezawa, X. Liu, W. Zhao, G. Zhao, and S. Woo, J. Phys.: Condens. Matter **32**, 143001 (2020).
[4] B. Göbel, I. Mertig, and O. A. Tretiakov, Phys. Rep. **895**, 1 (2021).
[5] S. Hayami and Y. Motome, J. Phys.: Condens. Matter **33**, 443001 (2021).
[6] M. Onoda, G. Tatara, and N. Nagaosa, J. Phys. Soc. Jpn. **73**, 2624 (2004).
[7] A. Neubauer, C. Pfleiderer, B. Binz, A. Rosch, R. Ritz, P. G. Niklowitz, and P. Böni, Phys. Rev. Lett. **102**, 186602 (2009).
[8] S. D. Yi, S. Onoda, N. Nagaosa, and J. H. Han, Phys. Rev. B **80**, 054416 (2009).
[9] K. Hamamoto, M. Ezawa, and N. Nagaosa, Phys. Rev. B **92**, 115417 (2015).
[10] Y. Shiomi, N. Kanazawa, K. Shibata, Y. Onose, and Y. Tokura, Phys. Rev. B **88**, 064409 (2013).
[11] Y. P. Mizuta and F. Ishii, Sci. Rep. **6**, 28076 (2016).
[12] K.-W. Kim, K.-W. Moon, N. Kerber, J. Nothhelfer, and K. Everschor-Sitte, Phys. Rev. B **97**, 224427 (2018).
[13] C. Jin, C. Zhang, C. Song, J. Wang, H. Xia, Y. Ma, J. Wang, Y. Wei, J. Wang, and Q. Liu, Appl. Phys. Lett. **114**, 192401 (2019).
[14] S. Huang, C. Zhou, G. Chen, H. Shen, A. K. Schmid, K. Liu, and Y. Wu, Phys. Rev. B **96**, 144412 (2017).
[15] M. Weißenhofer and U. Nowak, Phys. Rev. B **99**, 224430 (2019).
[16] T. Okubo, S. Chung, and H. Kawamura, Phys. Rev. Lett. **108**, 017206 (2012).
[17] A. O. Leonov and M. Mostovoy, Nat. Commun. **6**, 8275 (2015).
[18] S.-Z. Lin and S. Hayami, Phys. Rev. B **93**, 064430 (2016).
[19] S. Hayami, S.-Z. Lin, and C. D. Batista, Phys. Rev. B **93**, 184413 (2016).
[20] K. Mitsumoto and H. Kawamura, Phys. Rev. B **104**, 184432 (2021).
[21] K. Mitsumoto and H. Kawamura, Phys. Rev. B **105**, 094427 (2022).
[22] R. Ozawa, S. Hayami, and Y. Motome, Phys. Rev. Lett. **118**, 147205 (2017).
[23] S. Hayami, R. Ozawa, and Y. Motome, Phys. Rev. B **95**, 224424 (2017).
[24] A. N. Bogdanov and D. A. Yablonskii, Sov. Phys. JETP **68**, 101 (1989).
[25] S. Hayami and Y. Motome, Phys. Rev. Lett. **121**, 137202 (2018).
[26] S. Hayami and R. Yambe, J. Phys. Soc. Jpn. **89**, 103702 (2020).
[27] R. Yambe and S. Hayami, Phys. Rev. B **106**, 174437 (2022).
[28] O. I. Utesov, Phys. Rev. B **103**, 064414 (2021).
[29] O. I. Utesov, Phys. Rev. B **105**, 054435 (2022).
[30] H. D. Rosales, D. C. Cabra, and P. Pujol, Phys. Rev. B **92**, 214439 (2015).

[31] B. Göbel, A. Mook, J. Henk, and I. Mertig, Phys. Rev. B **96**, 060406(R) (2017).
[32] T. Shimokawa, T. Okubo, and H. Kawamura, Phys. Rev. B **100**, 224404 (2019).
[33] M. E. Villalba, F. A. Gómez Albarracín, H. D. Rosales, and D. C. Cabra, Phys. Rev. B **100**, 245106 (2019).
[34] H. D. Rosales, F. A. G. Albarracín, K. Guratinder, V. Tsurkan, L. Prodan, E. Ressouche, and O. Zaharko, Phys. Rev. B **105**, 224402 (2022).
[35] S. Ray and T. Das, Phys. Rev. B **104**, 014410 (2021).
[36] Y. H. Kwan, G. Wagner, N. Bultinck, S. H. Simon, and S. A. Parameswaran, Phys. Rev. X **12**, 031020 (2022).
[37] S. Hayami, Phys. Rev. B **105**, 014408 (2022).
[38] S. Hayami, Phys. Rev. B **105**, 184426 (2022).
[39] S. Hayami, J. Phys.: Condens. Matter **34**, 365802 (2022).
[40] K. Okigami, R. Yambe, and S. Hayami, J. Phys. Soc. Jpn. **91**, 103701 (2022).
[41] S.-Z. Lin, arXiv:2112.12850
[42] M. A. Ruderman and C. Kittel, Phys. Rev. **96**, 99 (1954).
[43] T. Kasuya, Prog. Theor. Phys. **16**, 45 (1956).
[44] K. Yosida, Phys. Rev. **106**, 893 (1957).
[45] Y. Akagi, M. Udagawa, and Y. Motome, Phys. Rev. Lett. **108**, 096401 (2012).
[46] B. Berg and M. Lüscher, Nucl. Phys. B **190**, 412 (1981).
[47] R. Ozawa, S. Hayami, K. Barros, G.-W. Chern, Y. Motome, and C. D. Batista, J. Phys. Soc. Jpn. **85**, 103703 (2016).
[48] R. Yambe and S. Hayami, J. Phys. Soc. Jpn. **89**, 013702 (2020).
[49] S. Okumura, S. Hayami, Y. Kato, and Y. Motome, J. Phys. Soc. Jpn. **91**, 093702 (2022).
[50] A. Mukherjee, D. S. Kathyat, and S. Kumar, Phys. Rev. B **105**, 075102 (2022).
[51] R. Yambe and S. Hayami, Sci. Rep. **11**, 11184 (2021).